Journal of Alloys and Compounds 759 (2018) 108–119

Contents lists available at ScienceDirect

Journal of Alloys and Compounds

journal homepage: http://www.elsevier.com/locate/jalcom

Aging behavior of an Al–Cu–Mg alloy

Ivan Zuiko*, Rustam Kaibyshev

Belgorod State University, Pobeda 85, Belgorod 308015, Russia

ARTICLE INFO

Article history:
Received 12 December 2017
Received in revised form
3 May 2018
Accepted 5 May 2018
Available online 11 May 2018

Keywords:
Aluminum alloy
Age-hardening
Mechanical properties
Microstructure
Phase transformations
Precipitations
Transmission electron microscopy

ABSTRACT

Effect of aging temperature on precipitation behavior and mechanical properties of an AA2519 alloy was examined. Long-term natural aging provides the best combination of strength and ductility by the precipitation of dense Guinier–Preston and Guinier–Preston–Bagaryatsky zones. This phenomenon, called "delayed hardening", has the same origin as the "rapid hardening" in AA2X24 alloys subjected to artificial aging. At 190 °C, high density of θ″-phase provides high strength. Peak aging is characterized by insignificant increase in strength associated with additional precipitation of θ′-phase. The overaging leads to the formation of precipitate structure dominated by θ′-phase. The formation of θ″- and θ′-phases can consume ~0.7 and ~3.3%Cu, respectively. Despite this, the number density of θ″-phase precipitates is higher than that of θ′-phase ones by a factor of ~40. The θ″-phase is effective strengthening agent in the AA2519 alloy. The Ω-phase plates with a very high aspect ratio (AR) > 100 precipitate during artificial aging.

1. Introduction

An AA2519 alloy (Al–5.6Cu–0.3Mn–0.3Mg–0.15Zr (wt. %)) exhibiting superior mechanical properties was developed as a new grade of the age-hardenable AA2219 alloy (Al–6.2Cu–0.3Mn–0.15Zr (wt. %)) [1–4]. Minor Mg addition and a reduced Cu content provide 20 and 100% increases in yield stress and total elongation, respectively, compared to those of the precursor [1,3–5]. Increased ductility and strength could be partially attributed to decreased volume fractions of primary θ-phase formed during solidification, since content of Cu in the AA2519 alloy approaches solubility of this element in Al matrix at a temperature of solution treatment and the positive effect of Mg on the precipitation structure. However, notwithstanding numerous works [6–12], the precipitation behavior of AA2519 alloy remains poorly known.

In Al–Cu–Mg alloys with high Cu/Mg ratio (≥5.6) the text-book precipitation sequence [13,14] occurs in supersaturated solid solution (SSSS):

$$SSSS \rightarrow GP\ zones(Al_3Cu) \rightarrow \theta''(Al_3Cu) \rightarrow \theta'(Al_2Cu) \rightarrow \theta(Al_2Cu) \quad (1)$$

Guinier–Preston (GP) zones consist of single layers of pure Cu atoms on $\{001\}_{Al}$ planes [13–15]. The θ″-phase comprises two $\{001\}_{Cu}$ layers separated by three $\{001\}_{Al}$ planes [1,13–15]. The θ″-phase may exist within the broad compositional range of 10–40 at.% Cu; therefore, different combinations of Cu and Al layers can form this phase. The most accepted structure of θ″-phase proposed by V. Gerold consists of two pure Cu layers separated by three Al layers along ⟨100⟩ [13,14]. The Gerold structure has superlattice and gives Al_3Cu stoichiometry rather than Al_2Cu and the orientation relationship of $\{001\}_{\theta''}||\{001\}_{Al}$ and $\langle 100\rangle_{\theta''}||\langle 100\rangle_{Al}$. In fact, the θ″-phase with this configuration is a multilayered structure of Cu atoms located on the $\{001\}_{\alpha}$ planes and separated by ~0.8 nm [14,15]. The θ″-phase exhibits plate-like shape with coherent broad faces, while the edges of the plates could be semi-coherent if the plates are relatively thick [1,13,14]. The θ″-platelets form by direct transformation from solute clusters or GP zones in the underaged condition and, therefore, their distribution is uniform [1,13,14].

The transition θ′-phase having the nominal stoichiometry of Al_2Cu and a bct structure ($I\bar{4}m2$, $a = 0.404$ nm, $c = 0.580$ nm), forms as rectangular or octagonal plates on $\{100\}_{Al}$ planes and also obeys the orientation relationship ($\{100\}_{Al}||\{100\}_{\theta'}$, $\langle 001\rangle_{Al}||\langle 001\rangle_{\theta'}$) [1,6–18]. Finely dispersed θ′-phase platelets are considered as an extremely shear-resistant precipitate [18]. The θ′-phase has coherent broad faces and semi-coherent interfaces at their peripheries [13–18]. The θ′-phase often forms on dislocations to

* Corresponding author.
E-mail addresses: zuiko_ivan@bsu.edu.ru, zuiko.ivan@gmail.com (I. Zuiko), rustam_kaibyshev@bsu.edu.ru (R. Kaibyshev).

https://doi.org/10.1016/j.jallcom.2018.05.053
0925-8388/

reduce the misfit in two $\langle 100\rangle_{Al}$ directions during peak aging and, therefore, its distribution is non-uniform [13,19]. Finally, the incoherent θ-phase is the thermodynamic equilibrium form of Al_2Cu with a body-centered tetragonal ($I4/mcm$, $a = 0.607$ nm, $c = 0.487$ nm) lattice.

The Cu/Mg/vacancy complexes form effective nucleation sites for GP zones, enhancing their nucleation rate [20,21]. GP zones are transformed *in situ* to the θ″-phase [13,14]: therefore, trace Mg promotes precipitation of the θ″-phase. In addition to Seq. (1), in certain circumstances the second precipitation sequence may appear [6,14,16]:

$$SSSS \rightarrow \{111\}clusters \rightarrow \Omega(Al_2Cu) \rightarrow \theta \quad (2)$$

The Ω-phase is fully coherent with the Al-matrix, forming thin hexagonal-shaped plates on $\{111\}_\alpha$ planes [14,22]. It was assumed that the Ω-phase is the most effective strengthening phase in Al–Cu–Mg–Ag alloys [23]. The Ω-phase has orthorhombic (*Fmmm*, $a = 0.496$ nm, $b = 0.859$ nm, $c = 0.848$ nm) lattice [14,16] with extremely small differences in atomic coordinates to those of the equilibrium θ-phase and the orientation relationship of $(001)_\Omega||(111)_{Al}$ $[010]_\Omega||[10\bar{1}]_{Al}$. Ag and Mg monolayers are located at the broad interfaces of the Ω-phase plates to improve coherency by reducing the misfit strain of the phase in Al–Cu–Mg–Ag alloys with Cu/Mg of ~10 [24,25]. Ag-Mg co-clusters forming on the $\{111\}_{Al}$ planes act as heterogeneous nucleation sites for the Ω-phase and, therefore, its distribution is uniform [14,22,25,26]. Despite extensive investigations, the origin of the precipitation of the Ω-phase in Ag-free Al–Cu–Mg alloys with high Cu/Mg ratios (e.g. AA2519) remains unknown [6,14,16].

The main aim of the present study is to examine the precipitate structures of the AA2519 after different aging conditions in details to elucidate the origin and nature of the superior combination of strength and plasticity. In industrial practice the AA2519 properties are achieved through T87 processing, including solution treatment, quenching, cold working and subsequent artificial aging [2–4,6]. This work is a part of complex study of precipitation behavior of the AA2519 and deal with the examination of aging behavior without pre-straining after quenching. The second aim is to provide a set of quantitative data on number density and volume fraction of transition phases for a critical discussion of the microstructural design of Al–Cu–(Mg–Ag) alloys and the strengthening efficiencies of aforementioned transition phases. It was shown by direct transmission electron microscopy (TEM) measurements [18,22] that only minor portion of Cu solutes is consumed for the precipitation of the θ′- and Ω-phases under peak aging condition in Al–3Cu–0.05Sn and Al–5.6Cu–0.72Mg–0.5Ag alloys. This data contradict the classical positions of the metastable solvus lines of the θ′- and θ″-phases, GP zones in Al–Cu binary phase diagram obtained by indirect hardness-reversion experiments, electric resistivity or X-ray measurements and quantitative nuclear magnetic resonance technique [13,14,18,27]. This contradiction arises from limited statistical data regarding the number density, size, shape, and distribution of transition phases in Al–Cu alloys acquired by TEM technique.

2. Experimental details

The AA2519 alloy, with a nominal chemical composition of Al–5.64Cu-0.33Mn–0.23Mg–0.15Zr-0.11Ti–0.09V–0.08Fe–0.08Zn–0.04Sn–0.01Si (in weight %), was manufactured by semi-continuous casting followed by homogenization annealing at 510 °C for 24 h [6,26]. Billets with dimensions of $55 \times 120 \times 155$ mm^3 were machined from ingots and swaged at a temperature of ~400 °C up to final dimensions of $41 \times 155 \times 160$ mm^3. Next, these billets were rolled with a total reduction of 75% (ε~1.3) at a temperature of 425 °C up to final thickness of 11 mm. Samples with dimensions of $10 \times 11 \times 20$ mm^3 and tensile specimens were cut from these plates and solution treated at 530 °C for 1 h and then immediately quenched in cold-water. This material condition is denoted here as supersaturated solution tempering (SST). Minor part of these samples was aged at ambient temperature (T4 temper) for times up to 2×10^3 h. Major part of these samples was aged at a temperature of 190 °C for times ranging from 3 min to 50 h (T6 temper). Quenching rate, bath temperature and heating rate to the aging temperature were the same for all specimens.

Samples for Vickers microhardness measurements were grounded, electrolytically polished and examined with a Wilson Wolpert 402MVD tester using a load of 2 N and dwell time of 10 s. At least 10 indentations were performed in arbitrarily selected areas for each data point to determine the average values and standard deviations of microhardness for each condition. Flat specimens of "dog bone" type with a 25 mm gauge length and a 3×7 mm^2 cross section were cut with a tensile axis matching with rolling direction. The uniaxial tensile tests to failure were carried out at ambient temperature using a screw-driven testing machine Instron 5882 equipped with an automatic high-resolution contacting extensometer MFX 500. The rate of cross-head displacement was constant (2 mm/min) and equivalent to an initial strain rate of 1.3×10^{-3} s^{-1}. Yield stress, ultimate tensile strength, uniform elongation and elongation-to-failure were calculated in accordance with ASTM E-8 standard. To ensure reproducibility, each reported value was averaged over tests of three samples at each experimental point.

Thin foils for TEM were produced by twin-jet electropolishing method described elsewhere [6,28]. JEOL JEM-2100 and Technai G^2 F20 microscopes operated at accelerating potential of 200 kV were used for TEM studies in bright and dark fields (BF and DF-TEM) modes. Precipitations of θ″ and θ′-phases were assessed directly by low magnification BF- and DF-TEM, respectively. To obtain reproducible and statistically meaningful data the quantitative measurements of precipitates diameter and thickness were averaged for $\geq 10^3$ measurements per each material condition. The experimental errors of precipitates diameters and thicknesses measurements are listed based on the particle size distribution (as standard deviation) and could be considered as veritable. Methodology for measurements of the number density per unit volume, the total volume fraction of particles, the limits of solid solubility of the θ′- and θ″-phases was reported in work [22]. The mass density of θ′ was calculated as 4.12 g/cm^3 whereas density of θ″ was taken to be slightly lower 4.04 g/cm^3. Values of dislocation density *via* X-Ray peak broadening were estimated according to modified Williamson-Hall method, following previous work [28].

Differential scanning calorimetry (DSC) was performed using a SDT Q600 (TA Instruments) calorimeter. The mass of the DSC samples was ~55 mg, and a protective atmosphere of pure argon was used. Samples after solution treatment followed by water quenching were heated from 20 to 600 °C at a rate of 2 °C/min. All DSC traces were corrected by subtracting a baseline obtained from a DSC run with empty pans. To confirm the authenticity of thermal effects we have scanned dilute aluminum.

3. Results

3.1. Initial microstructure

Initial structure is uniform (not shown here) with an average grain size of ~13 μm. Low-angle boundaries are aligned with the rolling direction predominantly and their portion is ~34%.

Dislocation density is $5.4 \pm 0.6 \times 10^{13}\ m^{-2}$. The primary particles precipitated during homogenization and solution treatments were described in detail in Ref. [28]. These particles are not expected to affect the precipitation of different phases during aging.

3.2. DSC analysis

Fig. 1 shows the DSC curves of the post-quenching AA2519 and a reference high-purity Al (5 N, 99.999) sample. The alloy curves are complex and clearly different from the differential heat capacity curves of the predecessor, AA2219 [29–33]. The following characteristics reaction regions are distinguished:

(i) At 71 °C, an exothermic reaction with the high energy released of 7.75 J g^{-1} is typically associated with the precipitation of GP zone in Al–Cu alloys. The formation of Cu-Mg co-clusters in Al–Cu–Mg alloys may also contribute to this peak [14,34–36]. Upon further heating the relatively weak endothermic reaction occurs between 72 and 86 °C.
(ii) Two exothermic reactions with low energy releases of 0.15 and 0.62 J g^{-1} at 102 and 203 °C may be attributed to the precipitation of θ″- and Ω-phase, respectively. It is worth noting the latter peak is typically attributed to the precipitation of Guinier-Preston-Bagaryatsky (GPB) zones in Al–Cu–Mg alloys with a Cu/Mg ratio of ~2.3 [14]. However, no precipitation of GPB zones was reported in alloys with high Cu/Mg ratio of >7. In the temperature interval of 205–220 °C the endothermic reaction may be attributed to the dissolution of θ″-phase.
(iii) At 242 °C, an exothermic θ′-phase precipitation reaction with a high energy release of 12.5 J g^{-1} occurs. No such exothermic reaction was observed in AA2219 alloy [30], although a similar reaction peak was observed in an Al–3.9 wt%Cu alloy at 275 °C [32].
(iv) At 258 °C, an endothermic θ′-phase dissolution reaction peak appears [30,37].
(v) In the temperature interval of 275–400 °C an exothermic θ-phase precipitation reaction peak appears [29,37].
(vi) The incipient melting point appears at 539 °C.
(vii) The onset of massive melting occurs at 578 °C.

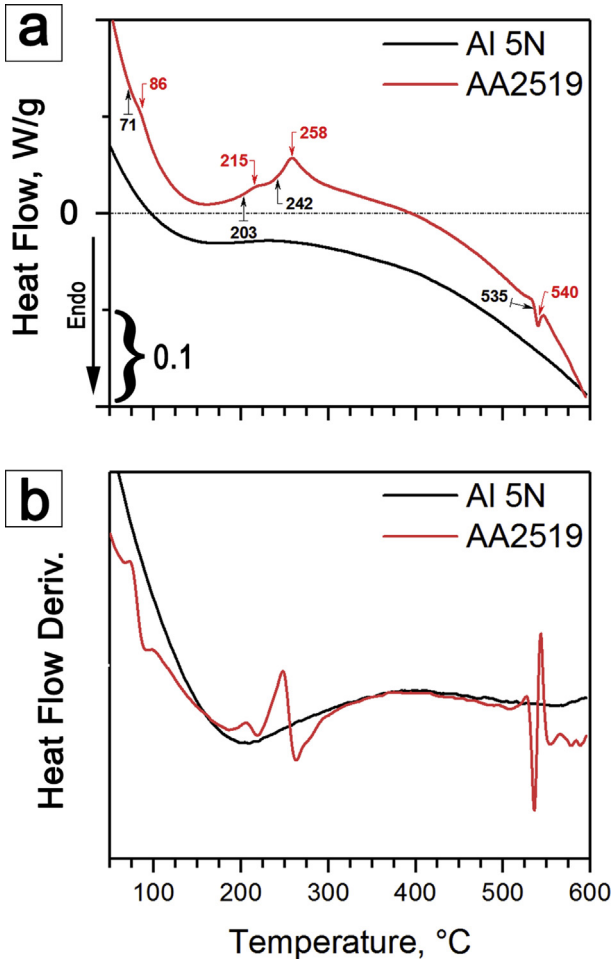

Fig. 1. The DSC curves of AA2519 and Al 5 N obtained at 2 °C/min. The black and red arrows indicate the onset of a reaction and peak temperatures, respectively. (For interpretation of the references to colour in this figure legend, the reader is referred to the web version of this article.)

Minor additives of Mg strongly promote the formation of the Cu-Cu clusters, Cu-Mg co-clusters and GP zones in the AA2519 alloy, compared to the AA2219 alloy or binary Al–Cu alloys, in which no distinct exothermic reactions was found at $T \leq 101$ °C [29–33,35,37]. It is apparent that the formation of Cu-Mg co-clusters, which differ distinctly from GP zones in their dimensions and free energy [21,36–38], and GP zones occurs at 71 °C, concurrently. The portion of energy released to form the clusters and GP zones is increased by ~42% and the exothermic peak appears at $\Delta T = 55$ K lower than that in AA2219 alloy and the Al–3.9 wt%Cu alloy [30,35]. In Al–Cu–Mg alloys with high Cu/Mg ratio the number density of Cu-Mg clusters is relatively low and these clusters tend to rapid dissolve under artificial aging [36]. Endothermic reaction between 72 and 86 °C could be attributed to dissolution of Cu-Mg co-clusters. S. Abis et al. [39] found this reaction in Al–Cu–Mg–Ag alloys with high Cu/Mg ratio and interpreted it in terms of GP zone dissolution. No well-defined endothermic reaction attributed to the dissolution of GP zones was found in AA2219 and the Al–3.9 wt%Cu alloy [29–33,35].

In AA2519 alloy the continuous GP → θ″-phase transformation takes place in the temperature interval of 103–201 °C that gives poor evidence for endothermic reaction. The relatively low scan rate employed (2 °C/min) allows the occurrence of this reaction. The upper temperature limit of GP zones stability in AA2519 is significantly lower than 200 °C that is a well-accepted upper limit for existence of GP zone in Al–Cu alloys [37]. The upper temperature limit of stability of θ″-phase of 230 °C in AA2519 and other Al–Cu alloys [33,37] is consistent. The precipitation of a low volume fraction of the Ω-phase promotes the dissolution of GP zones and precedes the precipitation of high volume fraction of the θ′-phase. This supports the statement that the free energy of the Ω-phase is higher than that of the θ′-phase [22]. In contrast with AA2219 [29,30,33], the precipitation of the θ′-phase is a distinctly independent reaction, characterized by a large energy release as in an Al–5.7 wt%Cu–0.5 wt%Mg–0.3 wt%Mn–0.15 wt%Zr alloy [40]. The temperatures of incipient and massive melting for AA2519 and AA2219 [29,30] are essentially the same. Thus the Mg additive affects the precipitation of all transient phases and has no effect on the precipitation of thermodynamically stable θ-phase and melting.

3.3. Mechanical properties

Fig. 2 shows the evolution of hardness as a function of aging time at 20 and 190 °C (T4 and T6 tempers, respectively). Immediately after quenching the hardness of the AA2519 alloy is low and equal to that of AA2219 alloy after natural aging [40]. At ambient temperature, the hardness remains unchanged for 25 h. Next the hardness increases by +4% as the aging time increased to 200 h.

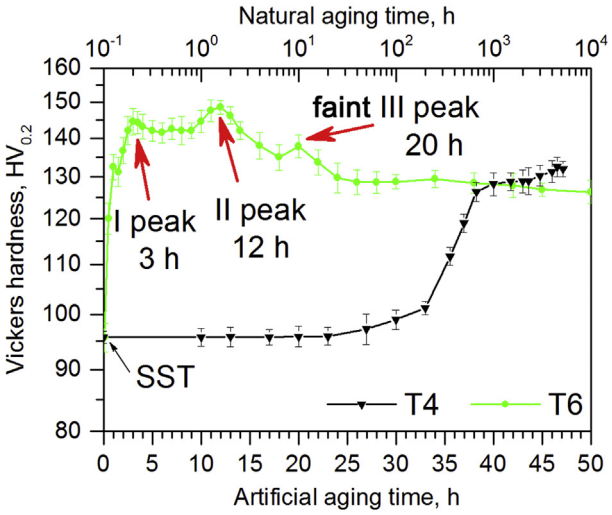

Fig. 2. The age hardening response of AA2519 alloy subjected to two different treatments. Red arrows indicate the positions of hardness peaks. (For interpretation of the references to colour in this figure legend, the reader is referred to the web version of this article.)

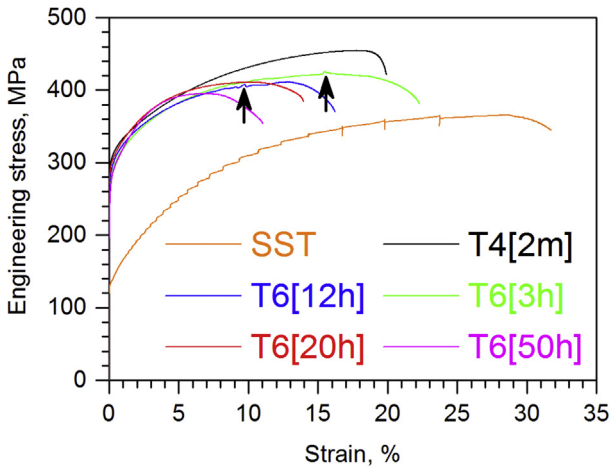

Fig. 3. Typical engineering stress-strain curves for AA2519 alloy in different conditions corresponding to the quenched material (SST), after long-term natural aging of 2 months (T4) and artificial peak aging with different times. The number in square brackets indicates the duration of the aging treatment. Black arrows indicate stress oscillations in the artificially aged specimens.

Then the hardness continues to increase as the aging time is increased up to 800 h; thereafter, it remains nearly unchanged with further aging. Minor Mg addition provides a +60% increase in hardness of AA2519T4 compared to that of AA2219T4 after long-term natural aging [31,32,40,41].

During artificial aging, a 40% increase in the microhardness occurs within 1 h. A peak aging hardness corresponding with a 50% increase in the hardness of the quenched material reaches after 3 h followed by a plateau from 5 to 15 h with a hardness of 141 ± 2 $HV_{0.2}$. Slight reversion is observed from 3 to 5 h and poor-defined second peak appears at 12 h. At times >15 h, upon further aging the hardness decreases remarkably. But at 20°h, third poor-defined hardness peak could be distinguished. It is worth noting that second and third hardness peaks are almost meaningless because their values are close to accuracy of measurement. However, the yield stress of specimens aged for 20 h is distinctly higher than after 18 and 22 (not shown here). During overaging, the hardness remains nearly constant. After 42 and 1000 h of artificial and natural aging, respectively, the hardness equilibrates. Character of age-hardening behavior in the AA2519 alloy is typical for AA2219 alloy, Al–5.76 wt %Cu alloy and Al–Cu–Mg(–Ag) alloys with high Cu/Mg ratio at T ≥ 140 °C [16,21,31,39,42]. The peak-aging hardness of the AA2519T6 is 6, 18 and 45% higher than those of an Al–5.76 wt%Cu [42], AA2219T6 [31] and a binary Al–5wt.%Cu alloy [43].

The typical engineering stress-strain (σ–ε) curves are shown in Fig. 3. The principal mechanical properties, namely microhardness, yield stress (σ_{YS}), ultimate tensile strength (σ_{UTS}), elongation-to-failure (δ), uniform elongation (ε_U) and σ_{YS}/σ_{UTS} ratio attributed to the work-hardening rate, are summarized in Table 1. All σ–ε curves exhibit continuous yielding followed by strain-hardening stage. Extensive initial strain hardening and overall parabolic shape of the σ–ε curves prior to necking are observed in the SST material. In the work-hardening stage, low-frequency stress oscillations attributed to dynamic strain aging (DSA) [26,44] are distinguished. The σ_{YS} of the SST material is very low, whilst the ductility and σ_{UTS} are high (Table 1). Long-term natural aging provides 124 and 30% increases in σ_{YS} and σ_{UTS} values, but δ is decreases by 43%. The σ–ε curve exhibits a prolonged strain-hardening stage and no serrations. As a result, the δ and ε_U values are nearly the same and sufficiently high.

The values of strength and ductility in the AA2519 alloy subjected to artificial aging are lower than those after long-term natural aging, despite the higher hardness. The work-hardening stage is shorter than that in the naturally aged material, σ_{YS} is almost independent of aging duration, and σ_{UTS} decreases with increases in aging time >20 h. Low-frequency Type A serrations [44] are observed (black arrows in Fig. 3) in the curves of samples aged up to 12 h. The overaged AA2519 exhibits lower elongation than peak-aged material does despite disappearance of plastic instability attributed to DSA. The values of σ_{YS}, σ_{UTS} and δ of the AA2519T6 alloy are higher than ones of AA2219T6 [31]. It is worth noting that the second hardness peak could be distinguished by higher values of σ_{YS} and σ_{UTS}.

The inspection of Tabor's relationship, $\sigma_{UTS} = c \times HV$ [42], shows (Table 1) that c for the long-term naturally aged alloy is somewhat higher than that for the artificially aged alloy. The c~3.2 MPa/$HV_{0.2}$ is often used as an empirical constant for metallic materials [45,46]. It is known [46] that high c values are attributed to strong work hardening. In the AA2519 subjected to long-term natural aging a high σ_{UTS} value appears despite relatively low hardness. The appropriate σ_{UTS} magnitude cannot be achieved in the artificially aged material because of the premature onset of plastic instability. Therefore, the long-term natural aging provides a superior combination of strength and plasticity in AA2519 alloy.

3.4. Precipitation microstructure

3.4.1. Natural aging

Fig. 4 shows typical TEM micrographs of naturally aged AA2519 alloy. The superlattice reflections on selected area diffraction (SAED) patterns, which were not emphasized by circles in Fig. 4 a–c, are attributed to the β and β′-phases ($Al_3(Zr,Ti)$) with non-coherent and coherent interfaces [26] and are unrelated to the transition phases precipitated during natural aging. Aging with a duration of ~1 h (SST condition) produces low-density GP zones, distinguished by continuous electron diffraction streaks through the {200} matrix spots parallel to the ⟨001⟩ directions, as well as a specific contrast indicating the presence of internal elastic stress fields originating from areas with dimensions of ~2 nm [6,14,47]. Very fine clusters and/or GP zones are precipitated uniformly on the $\{001\}_\alpha$ planes with increasing aging up to 72 h. Streaks are continuous and exhibit nearly uniform intensity that is indicative

Table 1
Room-temperature mechanical properties of aged AA2519 alloy.

Temper		Ageing time, h	Hardness, $HV_{0.2}$	σ_{YS}, MPa	σ_{UTS}, MPa	Elongation %		σ_{YS}/σ_{UTS}	c, MPa/$HV_{0.2}$
						ε_U	δ		
SST		<1	95.7 ± 1.1	136.2 ± 1.3	349.3 ± 2.1	22.1 ± 0.6	28.4 ± 1.4	0.390	3.6
T4		$>10^3$	128.3 ± 1.5	305.0 ± 1.0	455.0 ± 1.3	18.4 ± 0.5	19.9 ± 0.5	0.670	3.5
T6	I	3	144.5 ± 3.7	289.2 ± 0.5	425.7 ± 0.5	17.7 ± 0.5	21.4 ± 0.5	0.679	2.9
	II	12	148.5 ± 2.0	292.3 ± 0.5	408.8 ± 1.7	14.7 ± 0.5	16.3 ± 1.3	0.715	2.7
	III	20	137.8 ± 3.0	289.0 ± 1.0	410.7 ± 1.5	10.0 ± 0.5	13.6 ± 0.5	0.704	2.9
T6		50	126.3 ± 2.8	278.7 ± 0.5	393.7 ± 1.2	7.3 ± 0.3	10.6 ± 0.6	0.708	3.1

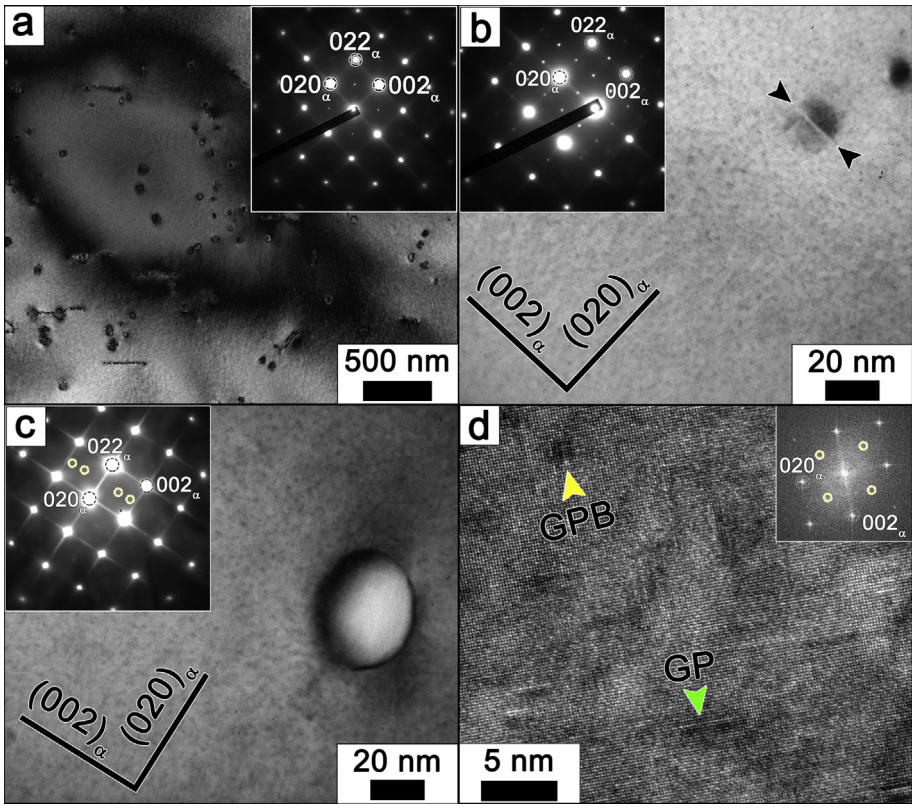

Fig. 4. BF-TEM micrographs with corresponding SAED patterns taken with the electron beam parallel to $\langle 001 \rangle_\alpha$ (a) SST. (b) natural aging for ~72 h. A "line of no contrast" indicated by a pair of black arrows within the coherent $Al_3(Zr,Ti)$ gives an evidence that the image is in focus. (c) after natural aging for ~1440 h. Spots from GPB-zones [14,47] are marked with green circles. (d) the HR-TEM image and corresponding FFT spectrum (inset) after natural aging for ~1440 h. (For interpretation of the references to colour in this figure legend, the reader is referred to the web version of this article.)

for dominance of single layer zones [48]. No distinct evidence was obtained for increasing number density of GP zones.

Long-term natural aging drastically increases the density of GP zones. The intensity of the streaks corresponding to zones is increased greatly with increasing aging duration (cf. insets in Fig. 4b and c). Streaks on SAED patterns become diffusive and exhibit none-uniform intensity associated with multilayer zones [48]. One of the striking features of the matrix spots in SAED patterns (Fig. 4c) is a marked asymmetry in intensity caused by compressive stresses in the matrix. The density of GP zones after 2000 h of natural aging is significantly higher, as indicated by stronger streaks, than that in AA2219 after 200 h natural aging or in a binary Al–5.5Cu after 5800 h natural aging [40,43]. Therefore, minor additives of Mg strongly increase number density of zones after long-term natural aging. In addition, bright spots marked with green circles in Fig. 4c appear.

A careful examination of more than five experimental SAED patterns and the high-resolution TEM (HR-TEM) images with corresponding fast Fourier transforms (FFT) provide conclusive evidence for GPB zones (inset of Fig. 4d) [14,34,49,50]. It is known [14,50–56] that the GPB zones are unique agglomeration with rod-like shape and fully coherent interface, 1–2 nm in diameter and 4–8 nm in length. Reports on the crystallographic structures of GPB zones are contradictory [14]. Generally, two different phases are spatially arranged in the shell and core regions of GPB zones, interpreted [50] in terms of GPB and GPBII phases, respectively. The GPBII comprise single or double units or agglomerates of two single units, with one-dimensional translational periodicity along the $\langle 100 \rangle_{Al}$ direction and may produce different characteristic diffraction spots in SAED patterns, depending on the type of the structural unit number [47]. Clear reflections are seen at $1/2[022]_\alpha$ in the FFT spectrum, as indicated by green circles (inset of Fig. 4d). These spots originate from GPBII zones [50–52,54,55]. The shell region produces streak reflections that create "half-crosses" outside the forbidden $\{110\}_{Al}$ reflections [50,51]. No such streaks were found (inset in Fig. 4d) and, therefore, GPB zones in AA2519 have only core

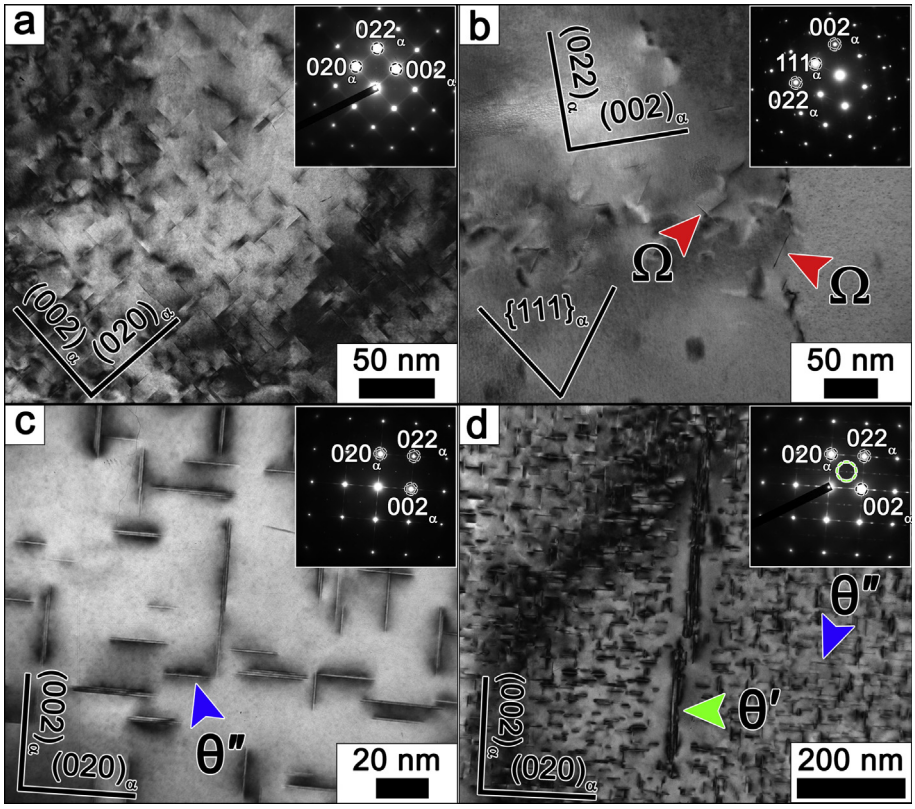

Fig. 5. BF-TEM micrographs and corresponding SAED patterns recorded near the $\langle 001\rangle_\alpha$ (a, c, d) and $\langle 011\rangle_\alpha$ (b) orientations from the aged for 0.5 h at 190 °C (a, b) and 3 h (c, d) AA2519 alloy. The blue, green and red arrows indicate θ″-,θ′- and Ω-phase plates, respectively. Note that the diffraction from the θ′-phase yields characteristics spots at the $\{220\}_\alpha$ positions, four $[101]_{\theta'}$ spots adjacent to the $\{220\}_\alpha$ positions marked by green circle and $\{002\}_{\theta'}$ spots [6,29]. (For interpretation of the references to colour in this figure legend, the reader is referred to the web version of this article.)

regions. Thus, the GPB zones precipitate along with dense GP zones in AA2519 after long-term natural aging in the Al–Cu–Mg alloy with high Cu/Mg~25. It is worth noting that GPB zones may precipitate in Al–Cu–Mg alloys with Cu/Mg ratio of ~2.3 upon high-temperature aging [50–54]. The formation of GPB zoned upon natural aging was reported in few works [53].

3.4.2. *Artificial aging*

Fig. 5 through 7 represent TEM micrographs of the alloy aged at 190 °C. The effect of aging duration on number density, volume fraction and dimensions of precipitates with the $\{001\}_\alpha$ habit plane is summarized in Table 2 and Fig. 8.

30 min of aging increases the density of GP zones and produces a limited number of θ″-phase, both formed on $\{001\}_\alpha$ planes as small plates [14,57] (Fig. 5a). The SAED patterns show continuous thin diffuse streaks of uniform intensity, parallel to $\langle 100\rangle_\alpha$, forming a characteristic network through the $\{200\}_\alpha$ and $\{220\}_\alpha$ matrix spots [14]. The staggered contrast of Fig. 5a is indicative for coherent stress originated from θ″/GP-zones. In addition, an insignificant number of the plate-like Ω-phase particles were precipitated on the $\{111\}_{Al}$ planes (Fig. 5b). The average diameter and thickness of the Ω-phase are 25.8 ± 11.7 and 0.79 ± 0.10 nm, respectively. It is worth noting that the corresponding SAED pattern according to $\langle 011\rangle_\alpha$ zone axis frequently did not include characteristic reflections, herewith precipitation of the Ω-particles is confirmed by their plate morphologies with their broad faces aligned along $\{111\}_\alpha$. The lack of specific diffraction spots is attributed to the low volume fraction of the phase. Platelets of both the θ″- and Ω-phases exhibit high aspect ratios (AR).

Increasing the aging time up to 3 h leads to dissolution of GP zones and the formation of a dense network of θ″-phase platelets (Fig. 5c and d, Table 2). The θ″-phase plates exhibit strong coherent stresses. On the SAED patterns, the θ″-phase platelets cause discontinuous $\langle 100\rangle_\alpha$ streaks through $\{200\}_\alpha$ positions with pronounced maxima at $\{200\}_\alpha$, as well as spot reflections at $\{220\}_\alpha$ positions from the precipitates whose broad faces are perpendicular to the beam [14]. Therefore, lattice of the θ″-phase consists of pure Cu layers separated by Al layers. In addition, the SAED and the simulated diffraction pattern for the Gerold model [6,14] are nearly the same. This indicates the superlattice of the θ″-phase and stoichiometry of Al_3Cu [14]. The volume fraction of the θ″-phase is low (Table 2). The distribution of the phase length is relatively narrow with a distinct peak at 17 nm (Fig. 8). In contrast, three peaks at 0.8, 1.2 and 1.4 nm are observed in distribution of plate thickness. The dimensions of the θ″-phase in AA2519 are significantly smaller than those in under-aged AA2219 [31–33,43], approaching the dimensions of the phase in binary Al–Cu alloys aged at the low temperature of 130 °C [57,58]. So, minor additions of Mg strongly refine particles of the θ″-phase providing a very high number density of this transition phase and facilitating the formation of distinct superlattice structure that exhibits distinct coherent stresses. Precipitation of the θ′-phase on dislocations (green arrow in Fig. 5d) leads to the formation of the θ″-phase free zones. The Ω-phase is also observed in the Al matrix (not shown here).

After 12 h aging, the non-uniform distribution of high-AR θ′-phase coexists with a uniform distribution of θ″-phase (Fig. 6, Table 2). An approximately three-fold increase in the volume fraction of the transition θ″/θ′-phases occurs as the time increases from 3 to 12 h by the precipitation of θ′-phase. The number density of the θ′-phase after 12 h aging is lower than that of the θ″-phase

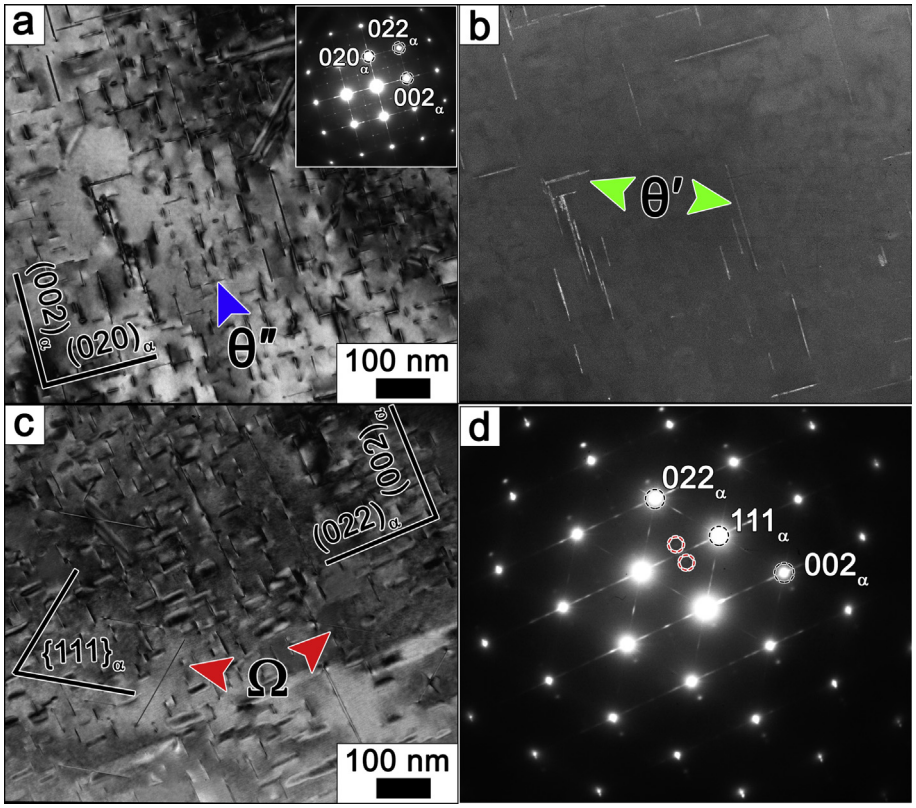

Fig. 6. TEM micrographs with corresponding SAED patterns of AA2519 after aging at 190 °C for 12 h. (a) BF-TEM with the $\langle 001\rangle_\alpha$ zone axis (b) DF-TEM taken using the $\{011\}_\alpha$ reflection corresponds to the same region at (a), (c) BF-TEM with the $\langle 011\rangle_\alpha$ zone axis, (d) SAED pattern taken from (c). A set of reflections at 1/3 and 2/3$\{022\}_\alpha$ (marked with red circles at d) as well as $(111)_\alpha$ diffuse striking were observed in the corresponding $\langle 011\rangle_\alpha$ SAED pattern (d), consistent with the unique precipitation diffraction from the Ω phase. The blue, green and red arrows indicate θ″-,θ′- and Ω-phase plates, respectively. (For interpretation of the references to colour in this figure legend, the reader is referred to the web version of this article.)

after 3 h aging by a factor of ~40; the θ″-phase platelets (blue arrow in Fig. 6a) exhibit coherent stresses. Therefore, after 12 h aging, the number density and volume fraction of the θ″-phase are significantly higher and lower, respectively, than those of the θ′-phase. These differences arise from the great difference in the dimensions of these phases. The distribution of the θ′-phase dimensions is nearly uniform (Fig. 8).

Two variants of plate-shaped precipitates lying on the $\{111\}_\alpha$ planes of the matrix was found (Fig. 6c and d). The SAED pattern clearly shows streaking along the $\langle 111\rangle_\alpha$ directions and distinct diffraction spots at the $1/3<022>_\alpha$ and $2/3<022>_\alpha$ positions, which confirm the presence of thin Ω-phase plates on the $\{111\}_\alpha$ matrix planes. Several ledges on the broad face of Ω are seen occasionally at high magnifications (not shown here). The average diameter and thickness of the Ω-phase plates are 116.8 ± 67.7 and 0.97 ± 0.21 nm, respectively. So, particles of the Ω-phase exhibit a very high AR exceeding 100. Despite this, number density of this phase is insignificant to affect mechanical properties. Therefore, we can conclude that the high strength could be provided by the mixture of θ″- and θ′-phases with a minor amount of the Ω-phase.

Further aging causes the complete dissolution of the θ″-phase, as confirmed by the SAED patterns (Fig. 7). The coarsening of the θ′-phase is insignificant. The volume fractions of both θ′- (Table 2) and the Ω-phases increase with increasing aging time. The decrease in hardness with increasing aging time is attributed to the replacement of the θ″-phase with particles of the θ′-phase. After 50 h aging this replacement is completed. Thus, overaging is associated with the almost complete dissolution of the θ″-phase. Note, that the large length and extremely small thickness of Ω-phase plates (see Figs. 6 and 7) is a unique feature of the AA2519 precipitation structure.

3.5. Fractography

SEM analyses of the fracture surfaces have been carried out on two tensile specimens, representing two of the aging conditions. As observed (Fig. 9), the aging temperature significantly affects the fracture mode. Long-term natural aged AA2519 shows transgranular ductile fracture with very fine dimples (Fig. 9a), whereas artificial aging causes mixed-type fracture. Large deep dimples are nucleated at particles and grain boundaries (Fig. 9b), while small dimples are observed at tear ridges. Transgranular ductile fracture is in dominance. However, evidence of both intergranular ductile fracture and transgranular brittle fracture modes was found.

4. Discussion

4.1. Precipitation structures

Inspection of the present experimental data shows that precipitation sequences in the AA2519 alloy at 20 and 190 °C are distinctly different. At ambient temperature, the following precipitation process occurs:

$$\text{SSSS} \rightarrow \text{GP zones} \rightarrow \text{GP} + \text{GPB zones} \quad (3)$$

No formation of GP zones was found upon natural aging in AA2219 alloy [59]. It is known [16,60], Mg atoms which have an atomic volume ~29% larger than Al atoms, give rise to an

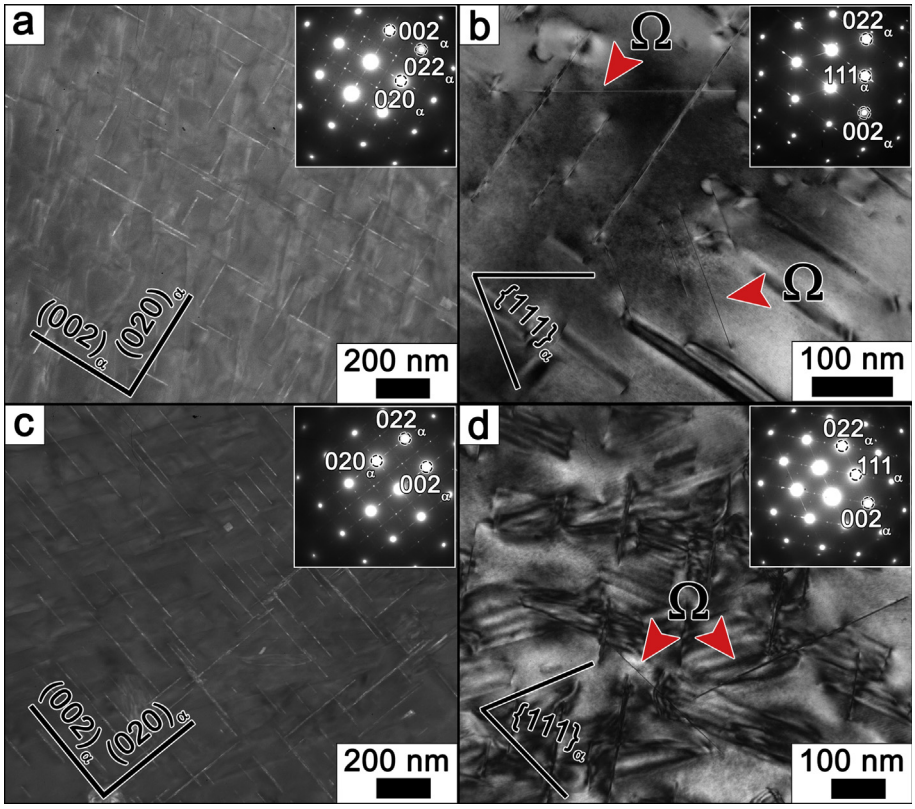

Fig. 7. Representative DF- and BF-TEM micrographs of AA2519 alloy aged for 20 h at 190 °C (a, b) and for 50 h at 190 °C (c, d). DF-TEM images (a, c) are picked up using $\{011\}_\alpha$ reflection. Note, the aspect ratio of Ω-phase precipitates is very high.

extensional distortion of the Al matrix. It seems to be appropriate in relieving the compressive strain normal to faces of single layer GP zones and θ″-phase and parallel to broad faces of θ″-phase [16,48,60]. The reliving of distortions decreases the misfit strain energy. Therefore, an increase Mg concentration decreases the nucleation barrier [13] for the formation of GP zones [59]. The second precipitation reaction in Seq. (3) is attributed to a very low Si content in the present AA2519 alloy. No formation of GPB zone was found in a grade of AA2519 alloy with Mg/Si~1.5 after several years of natural aging [59]. It is known [61] a high binding energy Si with Mg leads to the formation of Mg-Si clusters which are continuously enriched in Mg upon natural aging. No exothermic reaction (i) at 71 °C was found in AA2219 alloy and AA2519 alloy with 0.13 wt%Si [59]. Therefore, Mg addition and lowering Si strongly promote the formation of GP zones.

Long-term natural aging leads to the strong increase in the density of GP zones and additional precipitation of GPB zones providing a +47% increase in hardness, that is close to the effect of "rapid hardening" in Al–Cu–Mg alloys [36,56,62]. This phenomenon in AA2519 can be termed "delayed hardening" [36,50,56,62]. It is known [53,63] that the formation energy per solute (Cu + Mg) of GP, θ″-phase and GPBII are −0.21, −0.24 and ~-0.2 eV/atom. Therefore, GPB zone has a slightly lower negative energy than θ″-phase and the precipitation of GPB zone instead of θ″-phase takes place at room temperature due to lower activation energy barrier. Long time is required for the solutes to overcome diffusion distances for nucleation of GPB zones. Precipitation of GPB zone is accompanied by extensive precipitation of additional GP zones. Origin and nature of this phenomenon remain unknown. No delay hardening is observed in AA2219 alloy [32]. It is worth noting that long-term natural aging of the AA2519 alloy diminishes DSA, completely. Therefore, significant portion of solutes depleted from solid solution for precipitation of both GP and GPB zones.

At 190 °C, the precipitation sequences of (1) and (2) take place and no evidence for precipitation of θ'_{II}-phase having rod shape and the specific orientation relationship of $\{001\}_{\theta'}||\{110\}_{Al}$ $\langle 100\rangle_{\theta'}||\langle 001\rangle_{Al}$, S-phase and σ-phase ($Al_5Cu_6Mg_2$, P*m*3, $a = 1.999$ nm) [14,16,21] was found. Mg addition refines a

Table 2
Effect of aging time at 190 °C on characteristics of platelets precipitated on $\{001\}_\alpha$ planes. PAC and OAC mean peak and overaging conditions, respectively.

Ageing time, h		Plates dimensions, nm		Aspect Ratio	Number density,#/m^{-3}	Volume fraction, %
		diameter	thickness			
3 PAC I	θ″	21.0 ± 7.5	1.23 ± 0.36	17.15	$1.5 \pm 0.2 \times 10^{22}$	0.7 ± 0.2
12 PAC II	θ′	132.2 ± 76.6	4.45 ± 1.22	29.7	$4.0 \pm 0.3 \times 10^{20}$	2.4 ± 0.9
20 PAC III		133.3 ± 84.6	5.40 ± 1.49	24.67	$4.0 \pm 0.4 \times 10^{20}$	2.3 ± 0.7
50 OAC		132.5 ± 80.0	5.83 ± 1.85	22.71	$3.9 \pm 0.2 \times 10^{20}$	3.3 ± 0.8

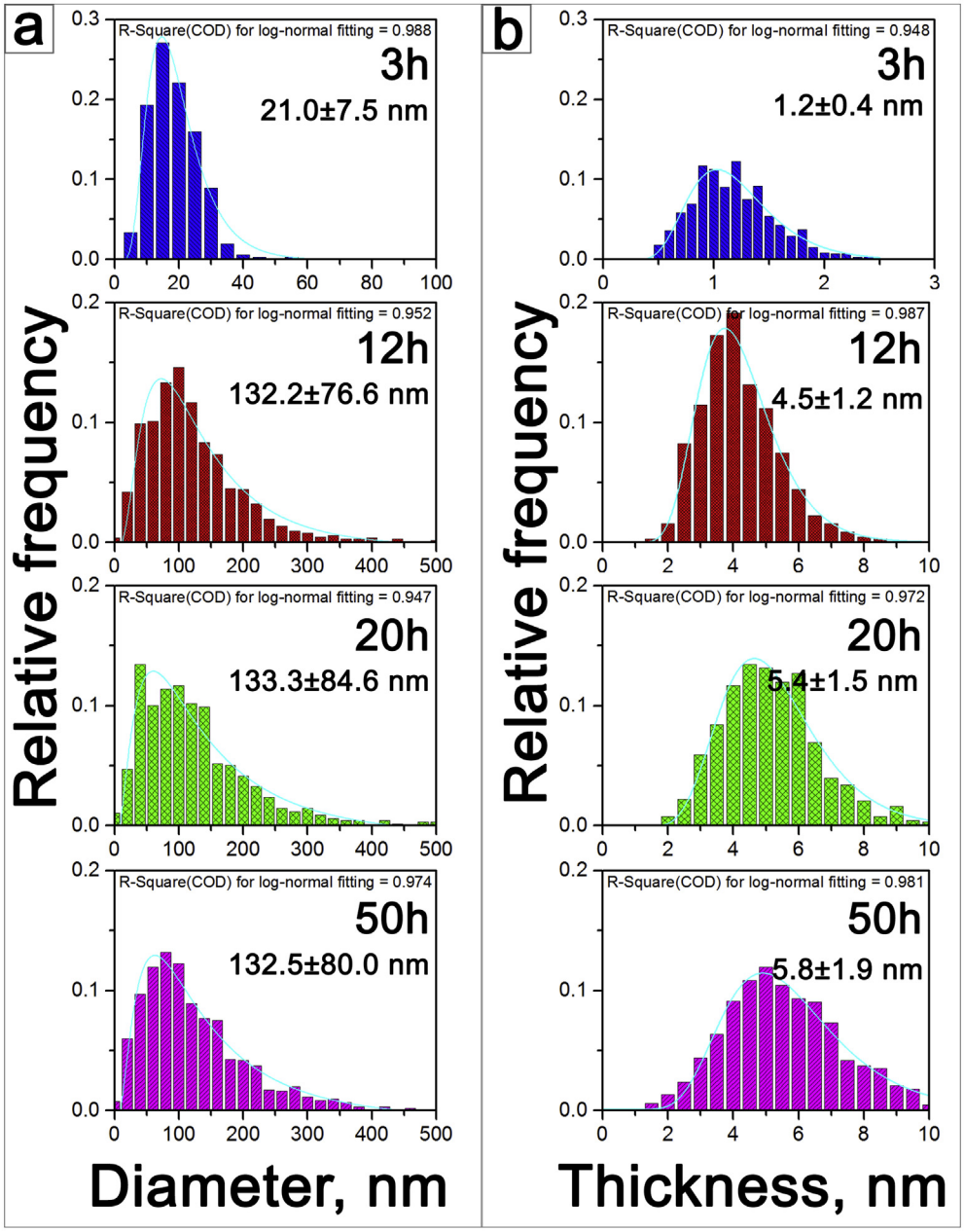

Fig. 8. Distribution of diameters (a) and thicknesses (b) of particles with plate-like shapes precipitated on $\{001\}_\alpha$ planes after aging.

dispersion of θ″-phase due to increased density of GP zones playing the role of nucleation sites for θ″-phase [59]. In addition, the reliving of distortion decreases the misfit strain energy of θ″-phase interfaces that reduces critical-size of nucleus [13]. The precipitation of Ω-phase in accordance with (2) leads to depletion of Mg atoms from Al matrix to interfaces of the Ω-phase that eliminates the reliving of compressive misfit of θ″-phase interfaces and increases strength due to coherent strengthening [38,64]. The peak aged AA2519 exhibits increased hardness in comparison AA2219 due to refinement of θ″-phase and the formation of mixture precipitation structure consisting of $\{001\}_\alpha$ and $\{111\}_\alpha$ platelets of θ″- and Ω-phase, respectively [18,19], at the onset of peak aging plateau. It is worth noting that no precipitation of Ω-phase was detected in AA2519 alloy with Mg/Si~1.5 showed lower strength in the peak aged condition [59] in comparison with the present AA2519. Si suppresses the formation of Ω-phase if the Mg/Si ratio (wt.%) is < 3 [65]. Therefore, Si is a detrimental impurity in AA2519 alloy.

Initially the nucleation of the θ′-phase is more likely to occur at quenched-in dislocations due to the associated lower nucleation barrier [13,63]. The replacement of uniformly distributed plates of the θ″-phase by the none-uniformly distributed θ′-platelets yields hardness plateau and poor defined second peak of hardness. Third hardness peak associates with the appearance of uniform distribution of the θ′-phase. It is known [21] that large Cu-rich clusters may play a role of precursors for θ′-platelets. However, the precipitation of dense θ″-phase platelets makes impossible retaining these clusters. Uniform nucleation of the θ′-phase is more likely to occur due to *in situ* transformation of θ″-phase interfaces [66]. This nucleation mechanism provides strong refinement of the θ′-phase in AA2519 alloy in comparison with AA2219 alloy and, therefore, increased strength.

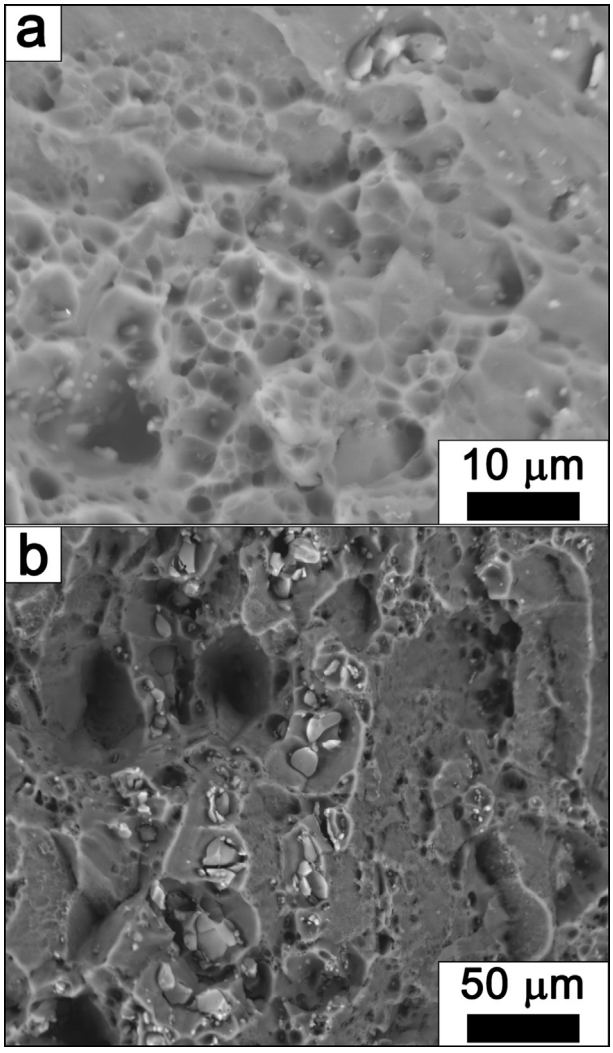

Fig. 9. Fracture morphologies of AA2519 alloy subjected to natural (a) and artificial (b) aging. The significantly different fracture mechanisms are evident.

4.2. Solvus lines of θ″- and θ′-phases

We have re-calculated the volume fraction of transition phases to content Cu solutes in Al matrix taking into account stoichiometry and density of θ″- and θ′-phases, and plotted the solvi of these phase in the Al-rich corner of binary Al–Cu diagram. Fig. 10 and Table 2 clearly show that the widespread metastable solvus curves for the θ″- and θ′-phases obtained by indirect experimental methods [13,14,27] are incorrect. The experimental data points are shifted to the left despite the fact that Mg decreases the solubility of Cu in Al [29,30,34,35,37]. Only ~14% of Cu is consumed for the formation of the θ″- phase and ~4.3 wt%Cu retains in solid solution at 190 °C. The small amount of Cu precipitated as θ″-phase provides a high hardness and strength. 50 h of artificial aging increases the amount of Cu consumed for the formation of the θ′-phases to ~3.3 wt%. Nearly the same values for the amount of Cu consumed for the formation of this phase were reported in works [18,22,67] after aging at 200 °C corroborating positions of metastable solvus curves for θ″- and θ′-phases at Fig. 10. Thus, a major portion of Cu may be precipitated in a form of θ′-phase. However, the strength of the AA2519 with precipitation structure consisting of the θ″-phase and mixed one consisting of θ″- and θ′-phases is essentially the same. Therefore, the specific strengthening efficiency of the shearable θ″-plates is greater than that of the non-shearable θ′-plates. This is explained by the high number density of the θ″-phase and the strong strengthening associated with coherent stress fields.

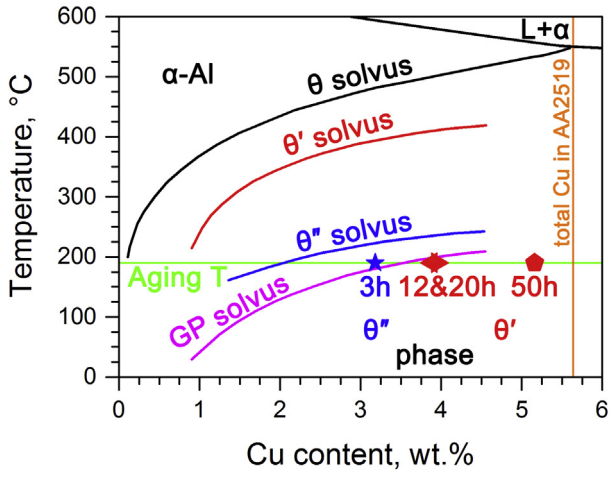

Fig. 10. Al-rich side of the Al–Cu binary phase diagram and corresponding solvi taken from Ref. [27]. The calculated points are plotted on the graph.

4.3. Effect of transient phases on mechanical properties

It is well known that the strength and ductility are usually inversely correlated. However, long-term natural aging provides the highest σ_{YS}, σ_{UTS}, ε_U and δ, concurrently. The HV/σ_{YS} ratios attributed to "delayed hardening" in AA2519 and "rapid hardening" in Al–2.5 wt%Cu–1.5 wt%Mg [36,68] are essentially the same. The combination of shearable GP zones and GPB zones, which are highly resistance to shearing, provides this hardening. Interaction of gliding dislocations with GP and GPB zones leads to continuous work-hardening that provides high uniform ε_U and achievement of high σ_{UTS}.

Analysis of mechanical properties shows that the highest strength, uniform elongation and ductility are attributed to the formation of three-dimensional networks of shearable θ″-phase plates on the $\{001\}_{Al}$ planes. The transition to a mixture of shearable θ″-phase and non-shearable θ′-phase plates has no effect on σ_{YS}, but decreases both elongation and σ_{UTS}. The full dissolution of shearable θ″-phase particles decreases both σ_{YS} and ductility (Table 1). The onset of premature fracture of artificially aged AA2519 occurs because of the decreased work-hardening ability. The appearance of intergranular and brittle fracture modes has a minor effect on the decreased ductility. Similar observations have been reported in AA2219 [40].

To evaluate the work hardening behavior, the tensile testing data were re-plotted in terms of true stress (σ), with the slope of the true stress-true strain plot ($d\sigma/d\varepsilon$) as a function of the true strain (ε) (Fig. 11). Three stage of work-hardening behavior [69,70] are distinguished: Stage I is a rapid decrease in work hardening; the transition from a linear to a parabolic dependence of $d\sigma/d\varepsilon$ on ε, takes place at Stage II; at Stage III, a sudden drop of work hardening occurs. Uniform tensile deformation occurs until the Considère criterion; i.e., when the $d\sigma/d\varepsilon$ is equal to the true stress σ, necking begins. Therefore, the transition from Stage II to Stage III has to occur at the applied stress determined by the Considère criterion for instability in numerous materials [69–71]:

$$d\sigma/d\varepsilon = \sigma. \quad (4)$$

The AA2519 alloy in SST shows a prolonged Stage II (Fig. 11a). In addition, the parabolic dependence of $d\sigma/d\varepsilon$ on ε generally transforms to a linear dependence with increasing strain. The onset of

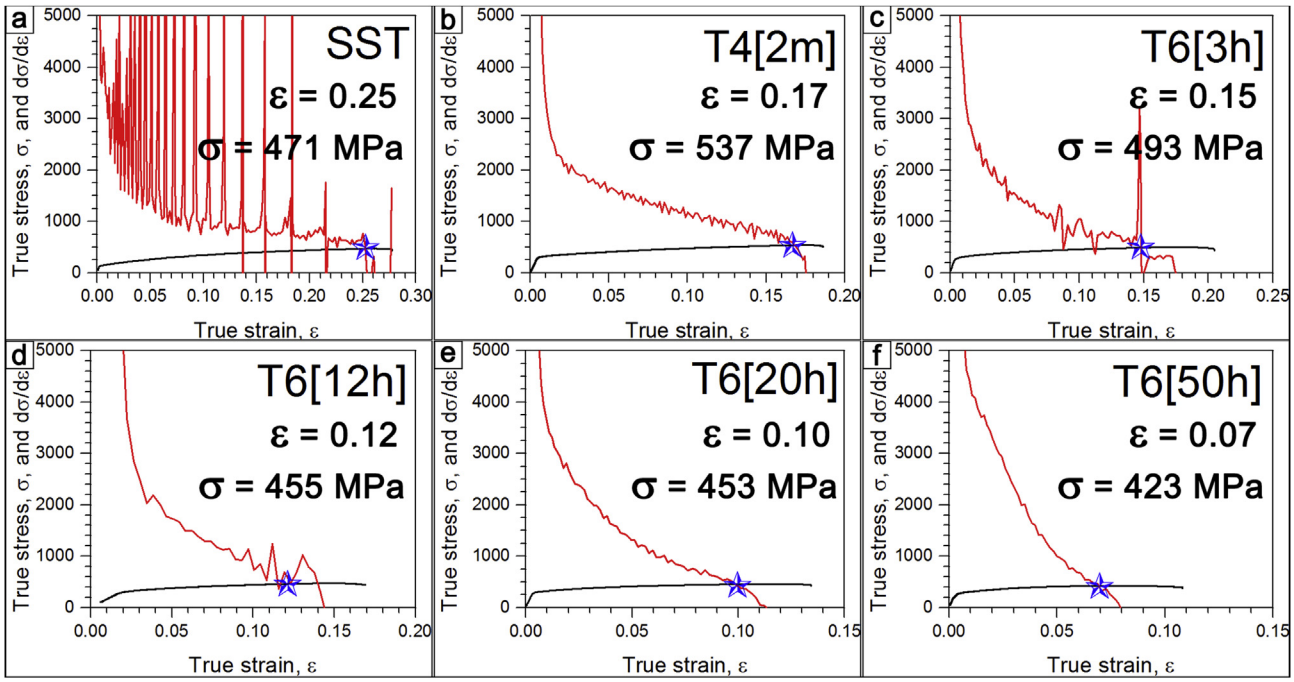

Fig. 11. Work hardening (red line) and true stress (black line) as a function of the true strain for AA2519 alloy. The numbers in square brackets denote the aging durations. The Considère criterion is marked by blue stars. (For interpretation of the references to colour in this figure legend, the reader is referred to the web version of this article.)

plastic instability occurs at $\sigma > d\sigma/d\varepsilon$ because of strong stress oscillations. DSA is responsible for the onset of necking at $d\sigma/d\varepsilon > \sigma$. Premature fracture attributed to Portevin-Le Chatelier effect has no relationship to σ_{UTS} and ductility. In AA2519 exhibiting "delayed hardening", the transition from Stage II to Stage III matches the Considère criterion and a pronounced linear Stage II is observed (Fig. 11b). As a result, the material achieves high σ_{UTS}, after which the onset of plastic instability occurs.

In contrast, Stage III is poorly-defined in artificially aged AA2519 (Fig. 11c–f). After 3 and 12 h aging, the onset of plastic instability is attributed to stress oscillations. After 20 and 50 h aging, Stage II is parabolic with a low rate of slowing down $d\sigma/d\varepsilon$ value with increasing ε. Transition through the Considère criterion has no remarkable effect on the dependence of $d\sigma/d\varepsilon$ on ε. Thus, premature fracture occurs in AA2519T6 by the loss of work-hardening ability at low strain. In addition, DSA facilitates the onset of plastic instability in peak-aged (3 and 12 h) AA2519.

5. Conclusions

We have investigated the mechanical properties and related precipitation structures in AA2519 after both natural and artificial aging. The major results are as follows:

1. Natural aging of AA2519 induces rapid precipitation of Guinier–Preston zones that have a slight effect on the mechanical properties. Long-term aging for approximately 1000 h causes a strong increase in the density of Guinier–Preston zones and the additional precipitation of Guinier–Preston–Bagaryatsky zones. This provides a superior combination of strength and plasticity: $\sigma_{YS} = 305$ MPa, $\sigma_{UTS} = 450$ MPa, ε_U~18%, δ ~20%. These properties are attributed to the pronounced work-hardening during tension. This phenomenon was termed "delayed hardening".
2. At 190 °C, the aging curve of the AA2519 alloy exhibits peak-aged plateau with two poor-defined peaks. At the onset of plateau for 3 h aging, the precipitation of the θ″-phase occurs. This precipitation structure provides the σ_{YS} of 290 MPa, σ_{UTS} of 425 MPa, ε_U of ~18%, δ of ~21%. The second maximum of hardness (after 12 h) associates with the mixed precipitation structure consisting of θ″- and θ′-phase. This precipitation structure provides σ_{YS} of 292 MPa, σ_{UTS} of 409 MPa, ε_U of ~15%, δ of ~16%. During overaging the θ′-phase replaces the θ″-phase.
3. Precipitation of the Ω-phase on $\{111\}_{Al}$ planes is observed in all artificially aged conditions. The specific features of this phase are a high AR (>100). The number density of Ω–phase plates is relatively low.
4. Analysis of the number density of θ″- and θ′-phases showed that the metastable solvi of these phase are located to the right of their generally accepted positions. The formation of θ″- and θ′-phases may consume ~0.7 and ~3.3%Cu, respectively. In the same time, the number density of θ″-phase is higher than that of θ′-phase by a factor of ~40.

Acknowledgments

This work is supported by the Ministry of Education and Science of the Russian Federation under the agreement № 14.584.21.0023 (ID number RFMEFI58417X0023). The authors are grateful to the staff of the Joint Research Center, «Technology and Materials» Belgorod State National Research University for their assistance with the mechanical and structural characterizations. I.Z. is thankful M. Gazizov for fruitful discussions and assistance with HR-TEM experiments.

References

[1] I.J. Polmear, Light Alloys: from Traditional Alloys to Nanocrystals, fourth ed., Elsevier/Butterworth - Heinemann, Oxford, Burlington, MA, 2006.
[2] J. Fisher, L.S. Kramer, J.R. Pickens, Aluminum alloy 2519 in military vehicles, Adv. Mater. Process. 160 (2002) 43–46.
[3] I. Crouch, The Science of Armour Materials, Woodhead Publishing, 2016.
[4] M. Handbook, MIL-DTL-4619C (MR) Aluminum alloy armor rolled plate (1/2 to 4 inches thick), weldable (alloy 2519), US Army Research Laboratory, 1998.
[5] R.F. Muraca, J.S. Whittick, Materials Data Handbook, Aluminum alloy, vol. 2219, Western Applied Research & Development, Inc, 1971, 1403 – 07, Industrial Road San Carlos, CA, 94070, USA.

[6] I.S. Zuiko, M.R. Gazizov, R.O. Kaibyshev, Effect of thermomechanical treatment on the microstructure, phase composition, and mechanical properties of Al–Cu–Mn–Mg–Zr alloy, Phys. Met. Metallogr 117 (2016) 906–919.
[7] L. Ye, G. Gu, J. Liu, H. Jiang, X. Zhang, Influence of Ce addition on impact properties and microstructures of 2519A aluminum alloy, Mater. Sci. Eng. A 582 (2013) 84–90.
[8] L. Ye, G. Gu, X. Zhang, D. Sun, H. Jiang, P. Zhang, Dynamic properties evaluation of 2519A aluminum alloy processed by interrupted aging, Mater. Sci. Eng. A 590 (2014) 97–100.
[9] Zh. Xin-ming, W. Wen-tao, Ch. Ming-an, G. Zhi-guo, J. Yu-zhen, Y. Ling-ying, Zh. Da-wei, L. Ling, K. Xiao-yue, Effects of Yb addition on microstructures and mechanical properties of 2519A aluminum alloy plate, Trans. Nonferrous Metals Soc. China 20 (2010) 727–731.
[10] J.Z. Liu, S.S. Yang, S.B. Wang, J.H. Chen, C.L. Wu, The influence of Cu/Mg atomic ratios on precipitation scenarios and mechanical properties of Al–Cu–Mg alloys, J. Alloys Compd. 613 (2014) 139–142.
[11] Z. Gao, X. Zhang, M. Chen, Investigation on θ′ precipitate thickening in 2519A-T87 aluminum alloy plate impacted, J. Alloys Compd. 476 (2009) L1–L3.
[12] Wen-tao Wang, Xin-ming Zhang, Zhi-guo Gao, Yu-zhen Jia, Ling-ying Ye, Da-wei Zheng, Ling Liu, Influences of Ce addition on the microstructures and mechanical properties of 2519A aluminum alloy plate, J. Alloys Compd. 491 (2010) 366–371.
[13] D.A. Porter, K.E. Easterling, M. Sherif, Phase Transformations in Metals and Alloys, third ed., CRC Press, 2009.
[14] S.C. Wang, M.J. Starink, Precipitates and intermetallic phases in precipitation hardening Al–Cu–Mg–(Li) based alloys, Int. Mater. Rev. 50 (2005) 193–215.
[15] A. Biswas, D.J. Siegel, C. Wolverton, D.N. Seidman, Precipitates in Al–Cu alloys revisited: atom-probe tomographic experiments and first-principles calculations of compositional evolution and interfacial segregation, Acta Mater. 59 (2011) 6187–6204.
[16] S.P. Ringer, B.T. Sofyan, K.S. Prasad, G.C. Quan, Precipitation reactions in Al–4.0Cu–0.3Mg (wt.%) alloy, Acta Mater. 56 (2008) 2147–2160.
[17] L. Bourgeois, Chr. Dwyer, M. Weyland, Jian-Feng Nie, B.C. Muddle, Structure and energetics of the coherent interface between the θ′ precipitate phase and aluminium in Al–Cu, Acta Mater. 59 (2011) 7043–7050.
[18] J. da Costa Teixeira, D.G. Cram, L. Bourgeois, T.J. Bastow, A.J. Hill, C.R. Hutchinson, On the strengthening response of aluminum alloys containing shear-resistant plate-shaped precipitates, Acta Mater. 56 (2008) 6109–6122.
[19] J.F. Nie, B.C. Muddle, Strengthening of an Al–Cu–Sn alloy by deformation-resistant precipitate plates, Acta Mater. 56 (2008) 3490–3501.
[20] T. Sato, S. Hirosawa, K. Hirose, T. Maeguchi, Roles of microalloying elements on the cluster formation in the initial stage of phase decomposition of Al-based alloys, Metall. Mater. Trans. A 34 (2003) 2745–2755.
[21] Z.Q. Zheng, W.Q. Liu, Z.Q. Liao, S.P. Ringer, G. Sha, Solute clustering and solute nanostructures in an Al–3.5Cu–0.4Mg–0.2Ge alloy, Acta Mater. 61 (2013) 3724–3734.
[22] M. Gazizov, R. Kaibyshev, Precipitation structure and strengthening mechanisms in an Al–Cu–Mg–Ag alloy, Mater. Sci. Eng. A 702 (2017) 29–40.
[23] F.J. Nie, B.C. Muddle, Microstructural design of high strength aluminum alloys, J. Phase Equil. 19 (6) (1998) 543–551.
[24] S.J. Kang, Y.-W. Kim, M. Kim, J.-M. Zuo, Determination of interfacial atomic structure, misfits and energetics of Ω phase in Al–Cu–Mg–Ag alloy, Acta Mater. 81 (2014) 501–511.
[25] L. Reich, M. Murayama, K. Hono, Evolution of Ω phase in an Al–Cu–Mg–Ag alloy – a three-dimensional atom probe study, Acta Mater. 46 (1998) 6053–6062.
[26] S. Bai, Z. Liu, X. Zhou, P. Xia, S. Zeng, Mg-controlled formation of Mg-Ag co-clusters in initial aged Al–Cu–Mg–Ag alloys, J. Alloys Compd. 602 (2014) 193–198.
[27] J.L. Murray, The aluminium-copper system, Int. Met. Rev. 30 (1985) 211–234.
[28] I. Zuiko, R. Kaibyshev, Deformation structures and strengthening mechanisms in an Al–Cu alloy subjected to extensive cold rolling, Mater. Sci. Eng. A 702 (2017) 53–64.
[29] J.M. Papazian, A calorimetric study of precipitation in aluminum alloy 2219, Metall. Trans. A 12 (1981) 269–280.
[30] J.M. Papazian, Calorimetric studies of precipitation and dissolution kinetics in aluminum alloys 2219 and 7075, Metall. Trans. A 13 (1982) 761–769.
[31] H. Wang, Y. Yi, S. Huang, Influence of pre-deformation and subsequent ageing on the hardening behavior and microstructure of 2219 aluminum alloy forgings, J. Alloys Compd. 685 (2016) 941–948.
[32] V.M.J. Sharma, K. Sree Kumar, B. Nageswara Rao, S.D. Pathak, Studies on the work-hardening behavior of AA2219 under different aging treatments, Metall. Mater. Trans. A 40 (2009) 3186–3195.
[33] E.M. Elgallad, Z. Zhang, X.-G. Chen, Effect of two-step aging on the mechanical properties of AA2219 DC cast alloy, Mater. Sci. Eng. A 625 (2015) 213–220.
[34] S.C. Wang, M.J. Starink, Two types of S phase precipitates in Al–Cu–Mg alloys, Acta Mater. 55 (2007) 933–941.
[35] M.I. Starink, P. van Mourik, Cooling and heating rate dependence of precipitation in an Al–Cu alloy, Mater. Sci. Eng. A 156 (1992) 183–194.
[36] R.K.W. Marceau, G. Sha, R. Ferragut, A. Dupasquier, S.P. Ringer, Solute clustering in Al–Cu–Mg alloys during the early stages of elevated temperature ageing, Acta Mater. 58 (2010) 4923–4939.
[37] A.M. Zahra, C.Y. Zahra, K. Raviprasad, I.J. Polmear, Effects of minor additions of Mg and Ag on precipitation phenomena in Al–4 mass% Cu, Philos. Mag. A 84 (2004) 2521–2541.
[38] Q. Zhao, Cluster strengthening in aluminium alloys, Scr. Mater. 84–85 (2014) 43–46.
[39] S. Abis, P. Mengucci, G. Riontino, A study of the high-temperature ageing of Al-Cu-Mg-Ag alloy 201, Phil. Mag. A 67 (1993) 465–484.
[40] L. Del Castillo, E.J. Lavernia, Microstructure and mechanical behavior of spray-deposited Al-Cu-Mg(-Ag-Mn) alloys, Metall. Mater. Trans. A 31 (2000) 2287–2298.
[41] S. Mondol, T. Alam, R. Banerjee, S. Kumar, K. Chattopadhyay, Development of a high temperature high strength Al alloy by addition of small amounts of Sc and Mg to 2219 alloy, Mater. Sci. Eng. A 687 (2017) 221–231, https://doi.org/10.1016/j.msea.2017.01.037.
[42] P.P. Ma, C.H. Liu, C.L. Wu, L.M. Liu, J.H. Chen, Mechanical properties enhanced by deformation-modified precipitation of θ′-phase approximants in an Al-Cu alloy, Mater. Sci. Eng. A 676 (2016) 138–145.
[43] D. Mitlin, V. Radmilovic, J.W. Morris, U. Dahmen, On the influence of Si-Ge additions on the aging response of Al–Cu, Metall. Mater. Trans. A Phys. Metall. Mater. Sci. 34 (2003) 735–742.
[44] A. Mogucheva, D. Yuzbekova, R. Kaibyshev, T. Lebedkina, M. Lebyodkin, Effect of grain refinement on jerky flow in an Al–Mg–Sc alloy, Metall. Mater. Trans. A (2016) 2093–2106.
[45] D. Tabor, The Hardness of Metals, Clarendon Press, Oxford, 1951.
[46] S. Hamada, M. Nakanishi, T. Moriyama, H. Noguchi, Re-examination of correlation between hardness and tensile properties by numerical analysis, Exp. Mech. 57 (2017) 773–781.
[47] M. Karlík, B. Jouffrey, High resolution electron microscopy study of Guinier-Preston (GP1) zones in Al–Cu based alloys, Acta Mater. 45 (1997) 3251–3263.
[48] E. Matsubara, J.B. Cohen, The G.P. zones in Al-Cu Alloys-II, Acta Mater. 33 (1985) 1957–1969.
[49] A. Tolley, R. Ferragut, A. Somoza, Microstructural characterisation of a commercial Al–Cu–Mg alloy combining transmission electron microscopy and positron annihilation spectroscopy, Philos. Mag. A 89 (2009) 1095–1110.
[50] L. Kovarik, S.A. Court, H.L. Fraser, M.J. Mills, GPB zones and composite GPB/GPBII zones in Al–Cu–Mg alloys, Acta Mater. 56 (2008) 4804–4815.
[51] Zhongwei Chen, Shishun Li, Reinterpretation of precipitation behavior in an aged AlMgCu alloy, J. Mater. Sci. 49 (2014) 7659–7668.
[52] Mami Mihara, Calin D. Marioara, Sigmund J. Andersen, Randi Holmestad, Equo Kobayashi, Tatsuo Sato, Precipitation in an Al–Mg–Cu alloy and the effect of a low amount of Ag, Mater. Sci. Eng. A 658 (2016) 91–98.
[53] L. Kovarik, M.J. Mills, Ab initio analysis of Guinier–Preston–Bagaryatsky zone nucleation in Al–Cu–Mg alloys, Acta Mater. 60 (2012) 3861–3872.
[54] L. Kovarik, P.I. Gouma, C. Kisielowski, S. a. Court, M.J. Mills, A HRTEM study of metastable phase formation in Al–Mg–Cu alloys during artificial aging, Acta Mater. 52 (2004) 2509–2520.
[55] Y.L. Zhao, Z.Q. Yang, Z. Zhang, G.Y. Su, X.L. Ma, Double-peak age strengthening of cold-worked 2024 aluminum alloy, Acta Mater. 61 (2013) 1624–1638.
[56] A. Deschamps, T.J. Bastow, F. de Geuser, A.J. Hill, C.R. Hutchinson, In situ evaluation of the microstructure evolution during rapid hardening of an Al–2.5Cu–1.5Mg (wt.%) alloy, Acta Mater. 59 (2011) 2918–2927.
[57] M. Takeda, Y. Maeda, A. Yoshida, K. Yabuta, S. Konuma, T. Endo, Discontinuity of G.P. (I) zone and θ′-phase in an Al–Cu alloy, Scr. Mater. 41 (1999) 643–649.
[58] S.K. Son, M. Takeda, M. Mitome, Y. Bando, T. Endo, Precipitation behavior of an Al–Cu alloy during isothermal aging at low temperatures, Mater. Lett. 59 (2005) 629–632.
[59] R.K. Wyss, R.E. Sanders Jr., Microstructure-property relationship in a 2XXX aluminum alloy with Mg addition, Metall. Trans. A 19 (1988) 2523–2530.
[60] E. Matsubara, J.B. Cohen, The G.P. zones in Al-Cu Alloys-I, Acta Mater. 33 (1985) 1945–1955.
[61] V. Fallah, B. Langelier, N. Ofori-Opoku, B. Raeisinia, N. Provatas, Sh. Esmaeili, Cluster evolution mechanisms during aging in Al-Mg-Si alloys, Acta Mater. 103 (2016) 290–300.
[62] R.K.W. Marceaua, C. Qiu, S.P. Ringer, C.R. Hutchinson, A study of the composition dependence of the rapid hardening phenomenon in Al–Cu–Mg alloys using diffusion couples, Mater. Sci. Eng. A 546 (2012) 153–161.
[63] Y. Chen, Z. Zhang, Z. Chen, A. Tsalanidis, M. Weyland, S. Findlay, L.J. Allen, J. Li, N.V. Medhekar, L. Bourgeois, The enhanced theta-prime (θ′) precipitation in an Al-Cu alloy with trace Au additions, Acta Mater. 125 (2017) 340–350.
[64] M.R. Ahmadi, E. Povoden-Karadeniz, L. Whitmore, M. Stockinger, A. Falahati, E. Kozeschnik, Mater. Sci. Eng. A 608 (2014) 114–122.
[65] S. Abis, P. Mengucci, G. Riontino, Influence of Si additions on the ageing process of an Al–Cu–Mg–Ag alloy, Phil. Mag. A 70 (1994) 851–868.
[66] L. Bourgeois, N.V. Medhekar, A.E. Smith, M. Weyland, J.-F. Nie, C. Dwyer, Efficient atomic-scale kinetics through a complex heterophase interface, Phys. Rev. Lett. 111 (2013) 046102.
[67] F.J. Nie, B.C. Muddle, Strengthening of an Al–Cu–Sn alloy by deformation-resistant precipitate plates, Acta Mater. 56 (2008) 3490–3501.
[68] K. Ralston, N. Birbilis, M. Weyland, C. Hutchinson, The effect of precipitate size on the yield strength-pitting corrosion correlation in Al–Cu–Mg alloys, Acta Mater. 58 (2010) 5941–5948.
[69] D. Yuzbekova, A. Mogucheva, D. Zhemchuzhnikova, T. Lebedkina, M. Lebyodkin, R. Kaibyshev, Effect of microstructure on continuous propagation of the Portevine Le Chatelier deformation bands international, Int. J. Plast. 96 (2017) 210–226.
[70] M. Jobba, R.K. Mishra, M. Niewczas, Flow stress and work-hardening behaviour of Al–Mg binary alloys, Int. J. Plast. 65 (2015) 43–60.
[71] S.D. Antolovich, R.W. Armstrong, Plastic strain localization in metals: origins and consequences, Prog. Mater. Sci. 59 (2014) 1–160.